Probing the spatial distribution of high-angular-momentum Rydberg wave packets

B. Wyker,[1] S. Ye,[1] F. B. Dunning,[1] S. Yoshida,[2] C. O. Reinhold,[3,4] and J. Burgdörfer[2,4]

[1]*Department of Physics and Astronomy and the Rice Quantum Institute, Rice University, Houston, Texas 77005-1892, USA*
[2]*Institute for Theoretical Physics, Vienna University of Technology, Vienna, Austria*
[3]*Physics Division, Oak Ridge National Laboratory, Oak Ridge, Tennessee 37831-6372, USA*
[4]*Department of Physics, University of Tennessee, Knoxville, Tennessee 37996, USA*

We demonstrate experimentally and theoretically that the spatial distribution of high-angular-momentum Rydberg wave packets, and thus off-diagonal elements of the density matrix, can be probed in detail through extraction of the moments of the position distribution $\langle y^\lambda \rangle (\lambda = 1,2)$ from quantum beat revivals. Detailed knowledge of the position distribution allows precise manipulation of the wave packet which is demonstrated by the control of its n distribution.

I. INTRODUCTION

High-angular-momentum Rydberg atoms have numerous potential applications in, for example, information processing, cavity quantum electrodynamics, and precision spectroscopy [1–6]. These rely on the production of stationary circular states for which various techniques have been devised [7–11]. Recently, time-dependent near-circular wave packets have been realized by coherently exciting high-angular-momentum Rydberg states with $n \sim 300$ [12]. The wave packet is a partially coherent superposition of (non)degenerate states involving only a few n levels but about 70–80 (ℓ,m) states within each n level $(n \sim \ell \sim m)$. The resulting statistical ensemble, described by the density matrix ρ, features strong correlations between the complex phases of the angular-momentum states [13]. As a result, the wave packet can undergo strong transient spatial focusing creating a localized wave packet that travels in a near-circular orbit, its motion mimicking that of the classical electron in the original Bohr model of the hydrogen atom [14]. The evolution of the (spatially localized) wave packet can be monitored by measuring its average position coordinates $\langle x(t) \rangle$ and $\langle y(t) \rangle$ [12,15] (provided that its motion is confined to the xy plane), which oscillate sinusoidally and are phase shifted by $\pi/2$. Because several discrete n levels are involved, the oscillations in $\langle x(t) \rangle$ and $\langle y(t) \rangle$ display a series of collapses and revivals [16,17] that result from focusing and defocusing of the spatial distribution. Even though high-angular-momentum Rydberg atoms are sensitive to interactions with the environment, quantum revivals can be observed on microsecond time scales [18]. Here we show that detailed information on the spatial distribution of a near-circular wave packet (or, more generally, of an ensemble of such wave packets) can be extracted from the moments of the position distributions $\langle y^\lambda \rangle (\lambda = 1,2)$ and related to distinct classes of elements in the density matrix. Furthermore, we demonstrate both experimentally and theoretically how these moments can be extracted from the revival signals. The analysis is applicable not only to circular Rydberg wave packets but also to more general systems such as molecular wave packets [19]. The improved knowledge of the spatial distribution obtained in this manner permits precise manipulation of the wave packet. As an example, we demonstrate a protocol to narrow (or to widen) the energy (or n) distribution of a near-circular wave packet by applying a carefully tailored half-cycle pulse [20].

II. SPATIAL DISTRIBUTION OF BOHR WAVE PACKETS

A fully coherent ideal Bohr wave packet [21,22] corresponds to a superposition of circular states,

$$|\Psi_{\text{ideal}}(t)\rangle = \sum_{n=n_i-\delta n/2}^{n_i+\delta n/2} c_n e^{-i\Phi_n(t)} |\psi_{n,\ell=n-1,m=n-1}\rangle, \quad (1)$$

where c_n is the modulus of the complex expansion coefficient, $\Phi_n(t) = \Phi_n(0) + E_n t = \Phi_n(0) - t/(2n^2)$, and the quantum numbers n extend over a narrow range (δn) that is much smaller than their mean value n_i $(\delta n/n_i \ll 1)$. (Unless otherwise noted atomic units are used throughout.) Because the spherical harmonics for circular states are of the form $Y_\ell^\ell \sim (\sin\theta)^\ell$ [where $\theta = \arccos(z/r)$], the wave function is localized near the xy plane in a circle with radius $\sim n_i^2$. While the localization in the radial direction is independent of the expansion coefficients $c_n e^{-i\Phi_n(t)}$, the spatial distribution on the circle [i.e., the variation with azimuthal angle $\phi = \arctan(y/x)$] depends sensitively on the complex expansion coefficients. For example, a superposition of two circular states with adjacent n has an azimuthal angular distribution that can be written as

$$\int_0^\infty dr\, r^2 \int_0^\pi d\theta \sin\theta |c_n e^{-i\Phi_n(t)} \psi_{n,n-1,n-1}(\vec{r})$$
$$+ c_{n-1} e^{-i\Phi_{n-1}(t)} \psi_{n-1,n-2,n-2}(\vec{r})|^2$$
$$= A_0(n) + A_0(n-1) + 2A_1(n)\cos[\phi - \Delta\Phi_n(t)], \quad (2)$$

where $\Delta\Phi_n(t) \equiv \Phi_n(t) - \Phi_{n-1}(t)$ and the positive definite functions $A_j(n)$ $(j = 0,1)$ are given by

$$A_j(n) = c_n c_{n-j} \int_0^\infty dr\, r^2 \int_0^\pi d\theta \sin\theta\, R_n(r,\theta) R_{n-j}(r,\theta),$$
$$(3)$$

with $\psi_{n,n-1,n-1}(\vec{r}) = R_n(r,\theta) e^{i(n-1)\phi}$. The distribution Eq. (2) is localized and peaks at $\phi = \Delta\Phi_n(t)$. Generally, the wave packet in Eq. (1) contains several pairs of adjacent n levels and each pair is localized at some $\phi = \Delta\Phi_n(t)$. Only when the relative phases are independent of n, i.e., $\Delta\Phi_n(t) = \Delta\Phi$, is the wave packet as a whole localized at a single azimuthal angle $\phi = \Delta\Phi$ [23]. Taking into account its time dependence, $\Delta\Phi_n(t) = (E_n - E_{n-1})t + \Delta\Phi_n(0) \simeq \Omega_n t + \Delta\Phi_n(0)$, the wave packet travels along a circular orbit with angular velocity $\Omega_n \equiv E_n - E_{n-1} \sim (n - 1/2)^{-3}$. Due

to the n dependence of Ω_n, a wave packet involving a finite number of discrete n levels must undergo dispersion leading to spreading of the wave packet. At even later times, however, the various components of the wave packet can rephase (modulo 2π) leading to a periodic series of revivals [18].

The position and degree of localization of the wave packet can be characterized by the expectation value of its Cartesian coordinates. For example,

$$\langle y(t) \rangle \simeq \sum_n c_n c_{n-1} |\langle \psi_{n,n-1,n-1} | y | \psi_{n-1,n-2,n-2} \rangle|$$
$$\times \sin[\Omega_n t + \Delta\Phi_n(0)] \qquad (4)$$

and comprises a sum of oscillatory terms mimicking classical circular motion with frequency Ω_n. This implies that the Fourier transform of $\langle y(t) \rangle$ can be used to extract information on the amplitude-weighted modulus of the dipole matrix elements,

$$D_{n,n-1} = c_n c_{n-1} |\langle \psi_{n,n-1,n-1} | y | \psi_{n-1,n-2,n-2} \rangle|, \qquad (5)$$

and the localization angles $\Delta\Phi_n(t)$ associated with different pairs of adjacent n levels [13,24,25]. A key in this analysis is the interrelation between n and m (i.e., $m = n - 1$ for circular states). The localization of each n component at $\phi = \Delta\Phi_n(t)$ [Eq. (2)] leads to a correlation between n (or energy) and azimuthal angle ϕ. Due to their different frequencies Ω_n, each n level can be resolved through Fourier expansion.

The present analysis can be extended from the ideal circular wave packet, Eq. (1), to near-circular wave packets comprising a distribution of high-ℓ states, $\ell \sim n$, with values of $m = n - \mu$, where $\mu \ll n$:

$$|\Psi_\mu(t)\rangle = \sum_{n,\ell} c_{n,\ell}^\mu e^{-i\Phi_{n,\ell}^\mu(t)} |\psi_{n,\ell,m=n-\mu}\rangle. \qquad (6)$$

When the phase of the expansion coefficient is independent of ℓ (i.e., $\Phi_{n,\ell}^\mu \simeq \Phi_n^\mu$), the interferences between different m (and n) components survive after the summation over ℓ and can form an azimuthally localized distribution similar to that in Eq. (2).

This analysis can be further generalized from a pure state to a partially coherent wave packet made up of an ensemble of superpositions Eq. (6) with different values of μ. While each superposition has the strong correlation between n and m (i.e., $m = n - \mu$), it is still experimentally possible to store the correlation into such an ensemble as will be shown later. The initial ensemble is described by the density operator

$$\rho(0) = \sum_\mu P_\mu |\Psi_\mu(0)\rangle\langle\Psi_\mu(0)| \qquad (7)$$

(typically about 70 ℓ and m levels are involved in the ensemble). Accordingly, the expectation value of y can be written as

$$\langle y(t) \rangle \simeq \sum_\mu \sum_n P_\mu D_n^\mu(0) \sin\left[\Omega_n t + \Delta\Phi_n^\mu(0)\right], \qquad (8)$$

with

$$D_n^\mu(t) \simeq \sum_\ell P_\mu |\langle \psi_{n,l,n-\mu} | \Psi_\mu(t)\rangle\langle\Psi_\mu(t) | y | \psi_{n,l,n-\mu} \rangle|. \qquad (9)$$

This expression includes only the dominant dipole matrix elements ($\Delta n = \Delta \ell = \Delta m = \pm 1$) as all other elements ($\Delta n > 1$ or $\Delta \ell = -\Delta m$) are negligible. Only when the relative phases $\Delta\Phi_n^\mu(0)$ are nearly independent of μ do the corresponding off-diagonal elements of the density matrix give a sizable contribution to $\langle y(t) \rangle$.

The expectation value of y [Eqs. (4) and (8)] can provide only limited information on the localization of the wave packet. For example, when one coefficient c_n in Eq. (1) is nearly zero, the adjacent levels ($n \pm 1$) may become invisible. Consequently, the relative phases between the next-to-nearest-neighbor states, $\Phi_{n+1} - \Phi_{n-1}$, cannot be extracted. Also, such information cannot be extracted from the expectation value of the orthogonal coordinate, i.e., $\langle x(t) \rangle$. Due to the circular symmetry of the wave packet $\langle x(t) \rangle$ and $\langle y(t) \rangle$, while shifted in azimuth by $\pi/2$ from each other, behave similarly and possess nearly identical frequency spectra. However, as we now demonstrate, more complete information on the spatial distribution can be obtained by exploring the higher moments $\langle y^\lambda(t) \rangle$, $\lambda = 2,3,\dots$, of a single Cartesian coordinate. For example, the second moment for the wave packet in Eq. (6) is given by

$$\langle y^2(t) \rangle \simeq \sum_{n,\ell,\mu} P_\mu \big\{ \langle \psi_{n,\ell,n-\mu} | \rho(0) | \psi_{n,\ell,n-\mu} \rangle \langle \psi_{n,\ell,n-\mu} | y^2 | \psi_{n,\ell,n-\mu} \rangle$$
$$+ 2|\langle \psi_{n-1,\ell,n-\mu-1} | \rho(0) | \psi_{n+1,\ell+2,n-\mu+1} \rangle \langle \psi_{n+1,\ell+2,n-\mu+1} | y^2 | \psi_{n-1,\ell,n-\mu-1} \rangle| \cos\left[\Omega_n^{(2)} t + \Delta\Phi_n^{(2)}(0) + \pi\right] \big\}, \qquad (10)$$

where $\Delta\Phi_n^{(2)}(0) = \Phi_{n+1}(0) - \Phi_{n-1}(0)$ (as discussed earlier just the phases of the expansion coefficients that depend on n are measurable.) As in Eq. (9), only the dominant terms are included. In Eq. (10), $\Omega_n^{(2)} = E_{n+1} - E_{n-1}$, and in the limit $n \to \infty$, $\Omega_n^{(2)} \simeq 2\Omega_n$. Consequently, $\langle y^2(t) \rangle$ has two maxima within an orbital period. This behavior can be understood from the spatial distribution of the superposition between next-to-nearest-neighbor states

$$\int_0^\infty dr\, r^2 \int_{-1}^1 d(\cos\theta) \left| \sum_\ell \left[c_{n+1,\ell}^\mu e^{-i\Phi_{n+1}(t)} \psi_{n+1,\ell,m-\mu+1}(\vec{r}) + c_{n-1,\ell}^\mu e^{-i\Phi_{n-1}(t)} \psi_{n-1,\ell,m-\mu-1}(\vec{r}) \right] \right|^2$$
$$= B_0(n+1,\mu) + B_0(n-1,\mu) + 2B_2(n+1,\mu) \cos\left[2\phi - \Delta\Phi_n^{(2)}(t)\right], \qquad (11)$$

and

$$B_j(n,\mu) = \sum_{\ell,\ell'} c_{n,\ell}^\mu c_{n-j,\ell'}^\mu \int_0^\infty dr r^2 \int_0^\pi d\theta \sin\theta$$
$$\times \tilde{R}_{n,\ell,n-\mu}(r,\theta)\tilde{R}_{n-j,\ell',n-j-\mu}(r,\theta), \qquad (12)$$

and $\psi_{n,\ell,m}(\vec{r}) = \tilde{R}_{n,\ell,m}(r,\theta)e^{im\phi}$. Inspection of the cosine term reveals two maxima at $\phi = \Delta\Phi_n^{(2)}(t)/2$ and at $\phi = \pi + \Delta\Phi_n^{(2)}(t)/2$. These two peaks (separated by π) evolve at the same rate $\Delta\Phi_n^{(2)}(t)/2 \sim (\Omega_n^{(2)}/2)t$ resulting in contributions to the expectation value $\langle y^2(t)\rangle$ at twice the orbital period. Similar to the first moment, the population and the relative phase between $n \pm 1$ levels can be obtained from the Fourier transform of $\langle y^2(t)\rangle$. Extending this analysis to higher moments can reveal further information on the density matrix and even finer detail on the spatial distribution of the wave packet.

Direct experimental determination of the moments of a position coordinate presents a challenge. In the special case of (near) circular states, ionization induced by sudden turn-on, at $t = t_{\rm probe}$, of a probe field can provide a measure of the initial electron position distribution [15]. The evolution of this distribution can then be monitored by varying the turn-on time and observing the time dependence of the ionization (or survival) probability. The motion of the electron in the presence of the probe field is governed by the Hamiltonian

$$H = \frac{p^2}{2} - \frac{1}{r} + yF(t), \qquad (13)$$

with

$$F(t) = \begin{cases} 0 & (t < t_{\rm probe}), \\ F_y^{\rm probe} & (t > t_{\rm probe}). \end{cases} \qquad (14)$$

The energy transfer resulting from application of the probe pulse depends on the initial position $y(t = t_{\rm probe})$ of the electron. When the final energy $(E_n + yF_y^{\rm probe})$ lies above the potential barrier $(-\sqrt{2F_y^{\rm probe}})$ formed by the Coulomb and applied fields (the "Stark saddle"), i.e., when $y(t = t_{\rm probe}) > y_{\rm ion} = -E_n/F_y^{\rm probe} - \sqrt{2/F_y^{\rm probe}}$, the electron can be considered as ionized [15]. (Here and in the following $F_y^{\rm probe} > 0$ is assumed.) Consequently the survival probability is given approximately by the probability that the electron is initially located in the region $y < y_{\rm ion}$, which can be obtained by integrating the spatial distribution $\rho(\vec{r},t) = \langle\vec{r}|\rho(t)|\vec{r}\rangle$ over $y < y_{\rm ion}$. Equivalently, we can consider the portion of the electronic wave packet with $y > y_{\rm ion}$ as ionized. Assuming that $\rho(\vec{r},t)$ is localized in the xy plane around a circle with radius $r = n_i^2$, the y integral can be replaced by a ϕ integral as

$$P_{\rm ion}(t) \simeq \int_0^\infty dr r^2 \int_0^\pi d\theta \sin\theta \int_{\pi/2-\phi_{\rm ion}}^{\pi/2+\phi_{\rm ion}} d\phi \langle\vec{r}|\rho(t)|\vec{r}\rangle$$
$$\simeq 2\sum_{n,\mu} B_0(n,\mu)\phi_{\rm ion}$$
$$+ 4\sum_{n,\mu} B_1(n,\mu)\sin[\Omega_n t + \Delta\Phi_n(0)]\sin(\phi_{\rm ion})$$
$$+ 2\sum_n B_2(n,\mu)\cos[\Omega_n^{(2)}t + \Delta\Phi_n^{(2)}(0) + \pi]$$
$$\times \sin(2\phi_{\rm ion}), \qquad (15)$$

where $\phi_{\rm ion} = \arccos(y_{\rm ion}/n_i^2)$ and the functions B_j are given by Eq. (12). Equation (15) represents a harmonic series with the second and the third terms mirroring the time dependence of the first moment, $\langle y(t)\rangle$ [Eq. (4)], and the second moment, $\langle y^2(t)\rangle$ [Eq. (10)], respectively. By setting $y_{\rm ion} = 0$ (or equivalently $\phi_{\rm ion} = \pi/2$), the survival probability, $P_{\rm sp}(t) = 1 - P_{\rm ion}(t)$, closely approximates the time dependence of $\langle y(t)\rangle$ as the second harmonic (and all even-order harmonics) cancel. When $\Delta\Phi_n(t) = \Omega_n t + \Delta\Phi_n(0) = \pm\pi/2$, the azimuthal distribution is localized at $\phi = \pm\pi/2$ and $\langle y(t)\rangle$ attains its extreme values. On the other hand, with finite $y_{\rm ion}$, or equivalently, $\phi_{\rm ion} \neq \pm\pi/2$, nonvanishing second harmonic components become visible. They can be maximized for $\phi_{\rm ion} = \pm\pi/4$. Note that in order to resolve the different harmonic components the n distribution must be narrow so that terms in different harmonic orders do not overlap with each other in the frequency domain. In principle, even higher harmonics can be extracted from the survival probability. In practice, Fourier amplitudes decay quickly with harmonic order and render higher harmonics difficult to observe. Based on this analysis we consider the harmonic decomposition Eq. (15) as a reasonable approximation to the multipoles $\langle y^\lambda\rangle$ [Eqs. (4) and (10)] as will be demonstrated below.

III. PRODUCTION OF NEAR-CIRCULAR WAVE PACKETS

The creation of near-circular wave packets and analysis of their multipoles $\langle y^\lambda\rangle$ is undertaken using the apparatus shown in Fig. 1 [18,22]. Potassium atoms contained in a tightly collimated beam are photoexcited to selected Rydberg states using the crossed output of a frequency-stabilized, extra-cavity doubled Rh6G cw dye laser. Experiments are conducted in a pulsed mode. The output of the laser is chopped into a train of pulses of $\sim$1 μs in duration using an acousto-optic modulator. Following each laser pulse, the Rydberg atoms are manipulated (and subsequently probed) using a series of pulsed electric fields (directed along either the x or the y axis indicated) which are generated by applying voltage pulses to the two electrodes shown. Following the pulse sequence, the number of surviving atoms is determined by selective field ionization for which purpose a slowly rising voltage ramp (rise time $\sim$1 μs) is applied to the bottom plate. The resulting electrons pass through a mesh grid and are counted using a particle multiplier. Measurements in which no pulsed fields are applied
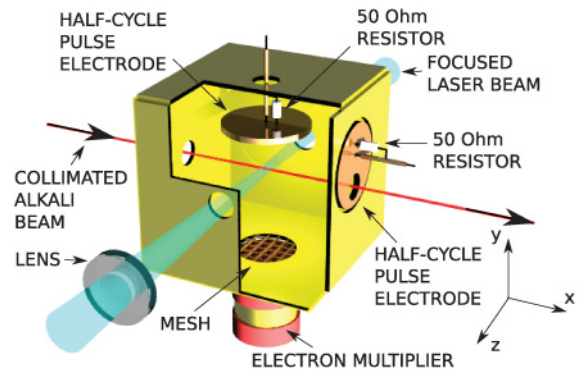

FIG. 1. (Color online) Schematic diagram of the apparatus.

are interspersed at routine intervals during data acquisition to monitor the number of Rydberg atoms initially being created which permits the fraction of Rydberg atoms that survive the pulse sequence, i.e., the survival probability, to be determined.

Creation of near-circular Bohr-like wave packets is a challenge since high-ℓ states are not directly accessible from low-ℓ ground states through absorption of one or even a few photons. Thus, in this work, we employ a method based on Stark precession which transforms strongly oriented quasi-one-dimensional (quasi-1D) low-ℓ Rydberg states (accessible from the ground state by a single photon) to circular states [26]. Extreme parabolic states oriented along the $+x$ or the $-x$ axis can be transformed to various elliptic states [27,28] by sudden application of a transverse "pump" electric field, F_y^{pump}, along the y axis. After a time $\pi/(3n_i F_y^{\text{pump}})$, i.e., a quarter of the Stark precession period, high-angular-momentum states Eq. (1) are formed. If, at this time, the pump field is suddenly turned off, further Stark precession is inhibited resulting in the formation of a near-circular wave packet comprising a coherent superposition of several n levels that then evolve freely in time.

Experimentally, it is challenging to generate single extreme parabolic states because the oscillator strength for their photoexcitation is small and Doppler broadening limits the available spectral resolution. In practice, an ensemble of quasi-1D high-n, $n \sim 300$, near-extreme parabolic states is created by direct photoexcitation from the ground state in the presence of a weak dc field. The creation of such Stark states can be optimized by properly choosing the strength of the dc field (~ 400 μV cm^{-1}) [29]. The laser frequency is tuned to $n_i \sim 305$ for which the energy difference between n_i and $n_i + 2$ states matches the splitting of the ground $F = 1$ and $F = 2$ hyperfine states, allowing their simultaneous excitation. This increases the photoexcitation rate and improves the statistical sampling of the data while the coherence of the initial ensemble is reduced. The dc field is then turned off and a transverse pump is applied. The experimentally generated wave packet is therefore made up of an ensemble of near-circular wave packets as described by the density matrix in Eq. (7). The spatial distribution of the product wave packet is analyzed using a probe field, F_y^{probe}, as described earlier.

IV. CALCULATED SPATIAL DISTRIBUTIONS

Before analyzing the (partially coherent) experimental wave packet we first examine the spatial distribution associated with the "ideal" Bohr wave packet derived from a single initial extreme "red-shifted" Stark state using both classical and quantum theory. Because full 3D quantum calculations are not feasible at the values of n, $n \sim 300$, studied experimentally, this is undertaken at $n = 150$.

The "classical" wave packet is obtained by simulating the pumping process, i.e., by solving the Liouville equation. A restricted microcanonical distribution is used to represent the initial $n = 150$, $k_x = -149$, $m_x = 0$ Stark state, which is oriented along the $-x$ axis. The pump field, $F_y^{\text{pump}} = 346$ mV/cm, is applied for a duration of 2.5 ns. The resulting classical phase-space probability density,

$$\tilde{\rho}_{\text{cl}}(x,y) = \int dz d^3 p\, \rho_{\text{cl}}(\vec{r},\vec{p}), \tag{16}$$

immediately following turn-off of the pump pulse (taken to define $t = 0$ in the following) is shown in Fig. 2(a), projected onto the xy plane. The wave packet is distributed nearly uniformly around a circle with an average radius of $\sim n_i^2$, forming a donut-shaped distribution. However, when the wave packet is decomposed into spectral components, i.e., energy bins, these are nonuniformly distributed around the circle. This is conveniently illustrated by considering the expectation value of the local principal action $\langle n(x,y) \rangle$ evaluated as

$$\langle n(x,y) \rangle = \frac{1}{\tilde{\rho}_{\text{cl}}(x,y)} \int dz\, d^3 p \sqrt{\frac{1}{2|H_{\text{at}}(\vec{r},\vec{p})|}} \rho_{\text{cl}}(\vec{r},\vec{p}) \tag{17}$$

[see Fig. 2(b)] where $H_{\text{at}} = p^2/2 - 1/r$. Those portions of the wave packet with the lowest energies (or actions n) are localized at azimuthal angles near $\phi \sim \pi/2$ and the highest energy components are localized near $\phi \sim -\pi/2$. This correlation between the principal action n and the azimuthal angle ϕ is caused by the energy transfer associated with the sudden turn-off of the pump pulse. As in the probing protocol Eq. (13), the energy transfer is determined by the initial electron position $y(t = 0)$. (Since the initial state is localized along the x axis little energy transfer occurs at turn-on of the pump pulse.) For $F_y^{\text{pump}} > 0$, the decrease in energy is maximal for electrons with $y \sim n_i^2$. In consequence, product states with the smallest values of n, $n_{\text{min}} \sim 147$, are localized near $\phi = \pi/2$. Similarly, states with the largest values of n, $n_{\text{max}} \sim 155$, are localized near $\phi = -\pi/2$. The various intermediate n levels are distributed symmetrically with respect to the y axis (i.e., at $\phi = \pi/2 \pm \alpha$).

As illustrated in Figs. 2(c) and 2(d), this n-ϕ mapping is also present in the quantum calculations. The quantum simulations are performed by numerically solving the time-dependent Schrödinger equation during the pump pulse. The resulting quantum distributions

$$\tilde{\rho}(x,y) = \int dz\, \rho(\vec{r},t = 0) \tag{18}$$

and

$$\langle n(x,y) \rangle$$
$$= \frac{1}{\tilde{\rho}(x,y)} \int dz\, \langle \vec{r}| \hat{n}^{1/2}\, \hat{\rho}(0)\, \hat{n}^{1/2} |\vec{r} \rangle$$
$$= \frac{1}{\tilde{\rho}(x,y)} \sum_{\mu} P_{\mu} \int dz\, \left| \sum_{n,\ell} \sqrt{n}\, c_{n,\ell}^{\mu}\, e^{-i\Phi_{n,\ell}^{\mu}(t)} \psi_{n,\ell,n-\mu}(\vec{r}) \right|^2 \tag{19}$$

closely resemble the classical distributions. As will be demonstrated, the extreme n levels, localized at $\phi = \pm\pi/2$, as well as the intermediate n levels, can be probed through harmonic analysis.

Consider now a mix of near-extreme red-shifted Stark states as is created experimentally. During the pump pulse (which acts like a $\pi/2$ pulse) each Stark state ($n = n_i, k_x = k_i, m_x = m_i$) is transformed to a near-circular Stark state ($n \simeq n_i, k \simeq -m_i, m \simeq -k_i$) [11]. Due to the nonadiabatic turn-on and -off of the pump pulse the final magnetic quantum number m is distributed within a finite range with $m \simeq n - \mu$ ($\mu \simeq n_i + k_i$). The same n-ϕ correlation persists for each near-circular state $|\Psi_\mu\rangle$, implying that the relative phases
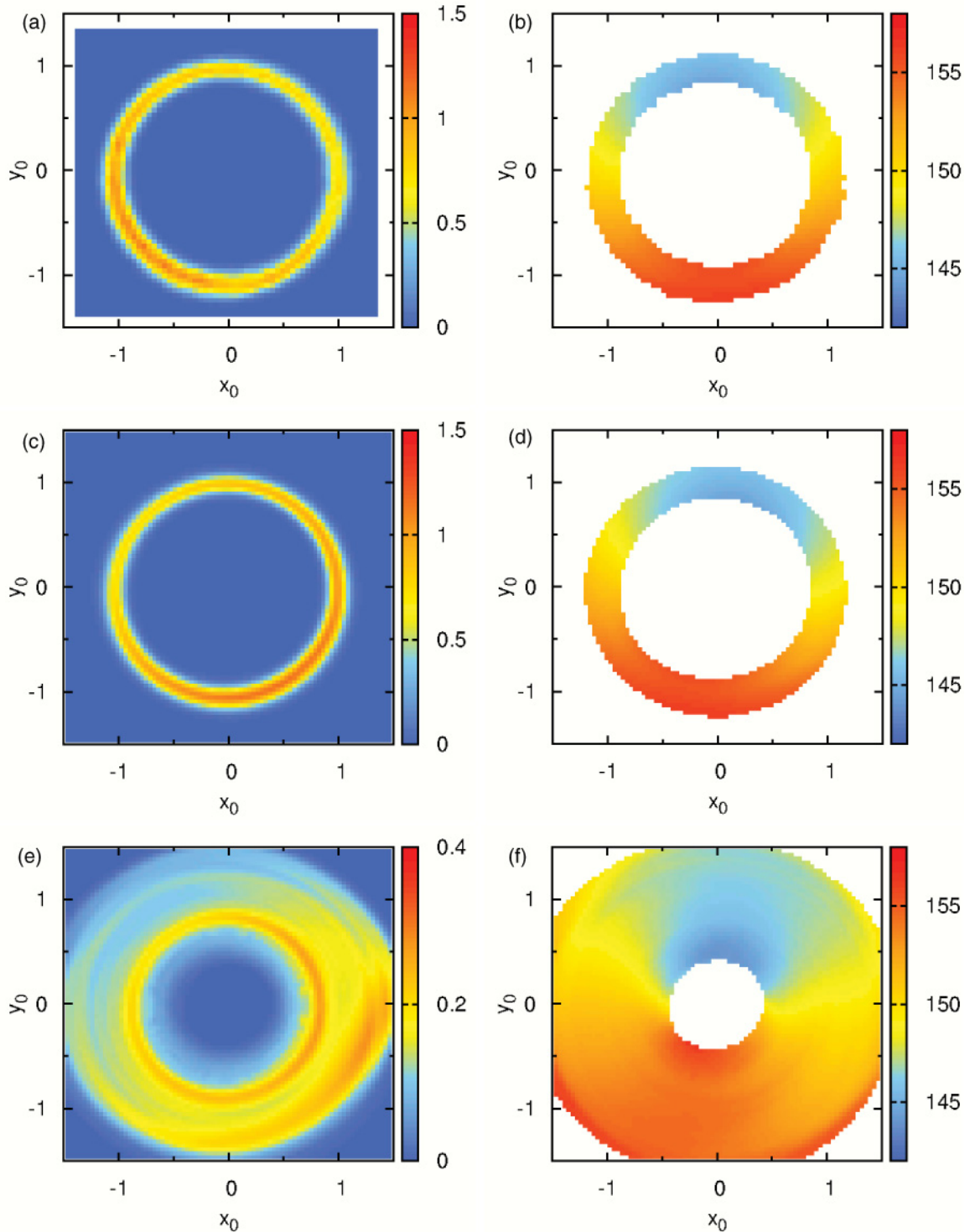
FIG. 2. (Color online) (a) Simulated spatial distribution (projected onto the xy plane) immediately following application of a 2.5-ns-long pump pulse of magnitude 346 mV/cm. The results are obtained by numerically solving the classical equations of motion for an initial ensemble comprising a restricted microcanonical ensemble modeling the extreme parabolic state with $n_i = 150$, $k_x = -149$, and $m_x = 0$. The corresponding average principal action $\langle n(x,y) \rangle$ evaluated locally at each position (x,y) is shown in (b). (c) and (d) Results obtained, for the same conditions, by numerically solving the time-dependent Schrödinger equation. (e) and (f) Results of quantum mechanical calculations for an initial state comprising an ensemble of near extreme parabolic states $n_i = 150$, $k_x = -117, -119, \ldots, -133$ (each equally populated), and $m_x = 0$ (see text). In all plots, the coordinates are in scaled units $x_0 = x/n_i^2$ and $y_0 = y/n_i^2$. $\langle n(x,y) \rangle$ is evaluated only at positions where the probability density $\tilde{\rho}(x,y)$ is larger than 0.01 (in scaled units) to avoid divergence with small denominators [see Eqs. (17) and (19)].

$\Delta\Phi_n$ and $\Delta\Phi_n^{(2)}$ depend only on n and are independent of ℓ and μ. This is illustrated by the quantum calculations presented in Figs. 2(e) and 2(f) for a partially coherent mix of near-extreme parabolic states ($n_i = 150$, $m_x = 0$, and values of k_x equally distributed between -117 and -133) that mimics the experimental protocol.

V. EXTRACTION OF MULTIPOLES

In this section we first analyze the extraction of multipoles $\langle y^\lambda \rangle$ using quantum simulations (at $n_i \sim 150$) chosen to mimic the experimental conditions. Survival probabilities obtained using Eq. (15) with $\phi_{\rm ion} = 2\pi/3$ and $\pi/2$ were determined during the free evolution and are presented in Figs. 3(a) and 3(b), respectively. (The choice $\phi_{\rm ion} = 2\pi/3$ matches the value used in the measurements.) The moments $\langle y(t) \rangle$ and $\langle y^2(t) \rangle$ of the simulated wave packet are shown in Figs. 3(c) and 3(d). The survival probabilities and $\langle y(t) \rangle$ display fast oscillations at the orbital period $T_{n_i} = 2\pi n_i^3$ (which sets the unit of scaled time.) As the wave packet involves a finite number of discrete n levels, a series of collapses and revivals in the oscillation amplitudes are observed as the various n components move in and out of phase. The Fourier transforms of the time signals
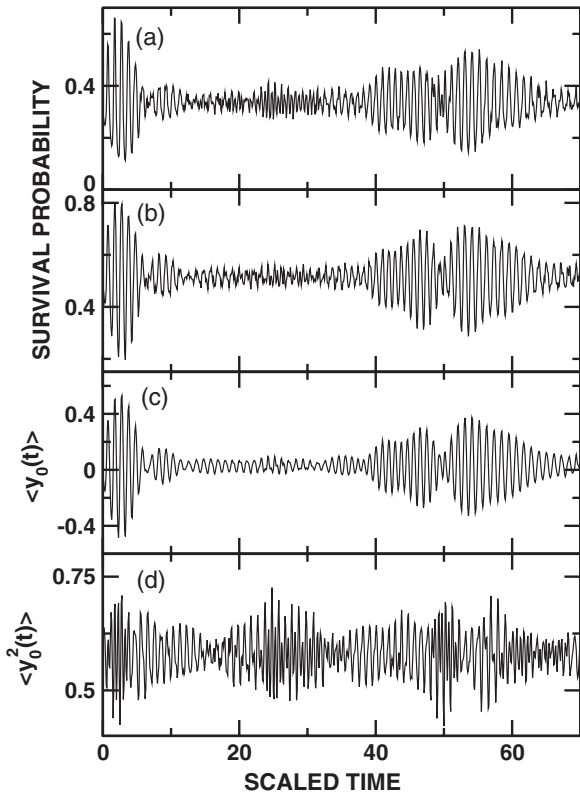

FIG. 3. (a) and (b) Survival probabilities Eq. (15) of the Bohr wave packet ($n_i = 150$) as a function of time of application of the probe pulse calculated according to Eq. (15) with $\phi_{\rm ion} = 2\pi/3$ and $\pi/2$, respectively. The results are obtained by numerically solving the Schrödinger equation. The pump pulse and initial state are the same as for Figs. 1(e) and 1(f). The unit of the scaled time is the Kepler period $2\pi n_i^3$ ($\simeq 513$ ps for $n = 150$) and that of the length is n_i^2. The expectation values of the moments $\langle y_0(t) \rangle$ [Eq. (4)] and $\langle y_0^2(t) \rangle$ [Eq. (10)] are presented in panels (c) and (d).

are shown in Figs. 4(a) to 4(d) and display a series of discrete peaks each of which corresponds to a contributing n level. As expected from Eqs. (4) and (10), the Fourier transforms of $\langle y(t) \rangle$ and $\langle y^2(t) \rangle$ are peaked around the first (Ω_{n_i}) and the second ($2\Omega_{n_i}$) harmonics. The survival probabilities also display multiple harmonics whose sizes depend on the choice of $\phi_{\rm ion}$ [Eq. (15)]. Detailed inspection of the first harmonic [see Fig. 4(e)] reveals a number of Fourier components whose phases are well localized. As seen in the calculated spatial distributions, the extreme product n levels ($n_{\rm max} \simeq 155$ and $n_{\rm min} \simeq 147$) are well localized in phase and contribute significantly to the Fourier spectrum. These components of the wave packet are initially localized (at $t = 0$) on opposite sides of the nucleus, i.e., at $\phi = -\pi/2$ for $n_{\rm max}$ and $\phi = \pi/2$ for $n_{\rm min}$ (Fig. 4). Thus the phase of the Fourier components acquires a direct geometric meaning in terms of initial azimuthal localization Eq. (2). In contrast, those components with intermediate values of n only appear prominently in the second harmonic spectrum, implying a symmetric spatial distribution with respect to the y axis Eq. (11). For the second harmonics, each contributing n level has a double-peaked distribution in ϕ [see Eq. (11)]. In Fig. 4(f), the plotted phase is divided by 2π and corresponds to $\Delta\Phi_n^{(2)}/2$ giving one of the two peak positions. For $n \sim 150$, this peak is initially positioned at $\phi = \Delta\Phi_n^{(2)}/2 \sim \pi$, the second peak being located at $\phi = \Delta\Phi_n^{(2)}/2 + \pi = 2\pi$, i.e., separated by π.

In general, the two angular peaks associated with the intermediate n levels are separated by an angle other than π. Their exact separation can be extracted by analyzing higher harmonic components of the survival probability for various values of the ionization threshold $\phi_{\rm ion}$. To extract information about a certain harmonic order the choice of $\phi_{\rm ion}$ is important [see Figs. 4(a) and 4(b)]. When $\phi_{\rm ion}$ is set to $\pi/2$, the contributions from double peaked spatial distributions in the survival probability are suppressed and the corresponding Fourier amplitudes become quite small [see Fig. 4(b)]. Accordingly, at intermediate n the specific phases extracted become unreliable. Observation of the second harmonics is facilitated by a different choice of $\phi_{\rm ion}$ (e.g., $\phi_{\rm ion} = 2\pi/3$). Alternatively, the second harmonic can be observed in the time domain [Figs. 3(a) and 3(b)]. At a scaled time of $\sim$20–30 the oscillations in the survival probability at the frequency of the first harmonic, i.e., the orbital frequency ($1/T_{n_i}$), collapse, allowing the frequency doubled oscillation to become visible, known as a 1/2 fractional revival [21]. The quantum simulations demonstrate that the first and second moments of the Cartesian coordinate y can be extracted from the first and second harmonic components of the survival probabilities. We now employ this tool to analyze experimental data for $n \sim 300$.

Measurements were undertaken with near-circular $n \sim 305$ wave packets obtained using a pump field $F_y^{\rm pump}$ of 10 mV cm^{-1} in amplitude and 42 ns in duration with rise and fall times of $\sim$300 ps, $\ll T_n$. Probe pulses $F_y^{\rm probe}$ of 6 ns in duration and with amplitudes of $\sim$104 and 76 mV cm^{-1} were employed to obtain average survival probabilities $\bar{P}_{\rm sp}$ of $\sim$50% [Fig. 5(a)] and $\sim$75% [Fig. 5(b)], respectively. The former enhances the first harmonics, the latter the second harmonics. The measured survival probabilities, recorded at intervals of $\sim$0.4 ns, revealed a series of strong quantum revivals. Fourier
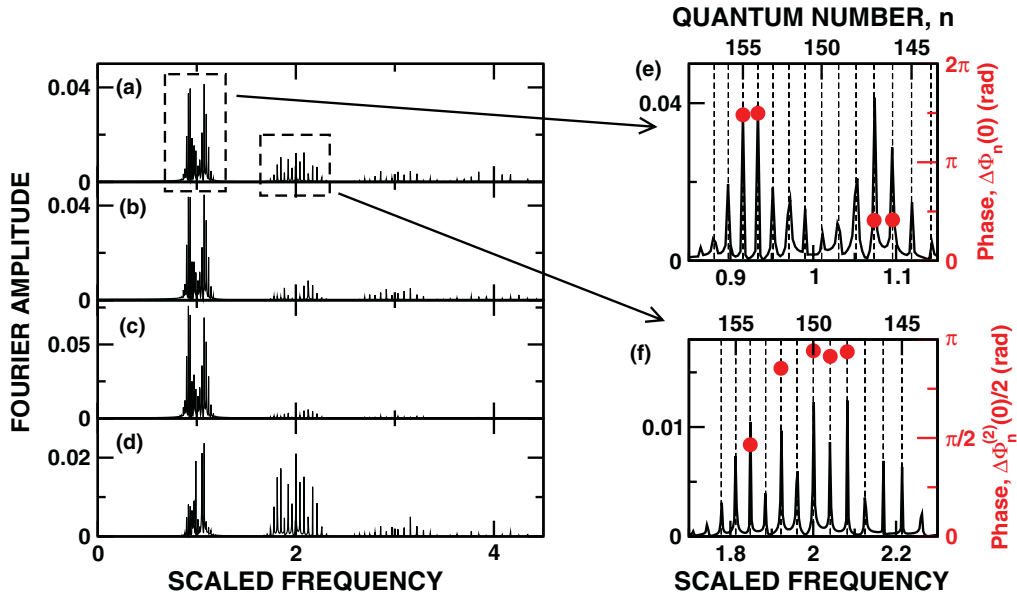
FIG. 4. (Color online) (a) to (d) Amplitudes of the Fourier transforms of the data in Fig. 3, shown in the same order. (e) and (f) Expanded views in the vicinity of the first and second harmonics. The dots indicate the phases of the complex Fourier coefficients for the dominant peaks (phase scale provided by the axes on the right). The conversion from frequency to the quantum number n [dashed lines and top axes in panels (e) and (f)] is done using $\omega_n = (n - 1/2)^{-3}$ and $\omega_n = 2n^{-3}$ for the first and second harmonics, respectively.

transforms of the data sets are presented in Figs. 6(a) and 6(b). The first harmonic spectrum peaks at $n \sim 302$–305 and 309–311. The phase of the Fourier expansion coefficients shows that the lower n levels are initially (at $t = 0$) located predominantly in the positive half-space ($y > 0$, $\phi \sim \pi/2$) whereas the higher-n states are positioned in the negative half-space ($y < 0$, $\phi \sim -\pi/2$), just as seen in Fig. 2. As noted earlier, the suppression of the Fourier amplitude in the vicinity of $n = 306$–308 should not be interpreted as an indication that the popula-

tion of the corresponding n levels is small. Indeed, the second harmonic spectrum [Fig. 6(b)] displays strong peaks at these intermediate n levels. Moreover, the phases of Fourier components show that the localization angles for these levels are near $\phi = 0$ [and π (Eq. (11)]; i.e., they correspond to excitation near $y \simeq 0$ and are nearly equally distributed at $x \simeq \pm n_i^2$. Since this
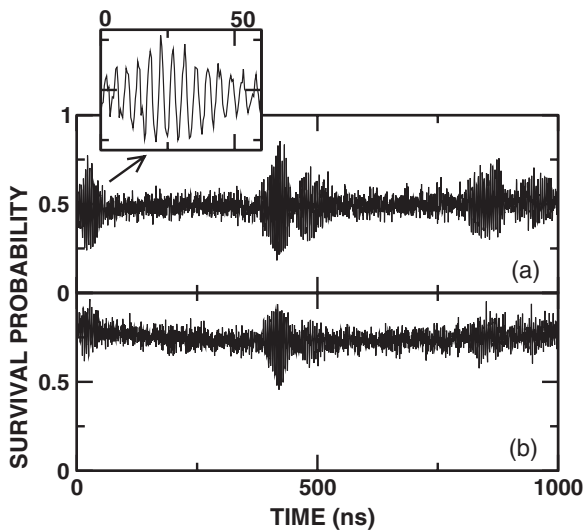

FIG. 5. Survival probabilities measured following sudden turn-off of a transverse 43-ns-long, 10 mV cm^{-1} pump pulse applied to a mix of quasi-1D $n_i = 304$ and 306 atoms (see text). Probe pulses of 6 ns in duration and amplitudes of (a) 104 mV cm^{-1} and (b) 76 mV cm^{-1} are employed. The inset illustrates the data on a finer scale.
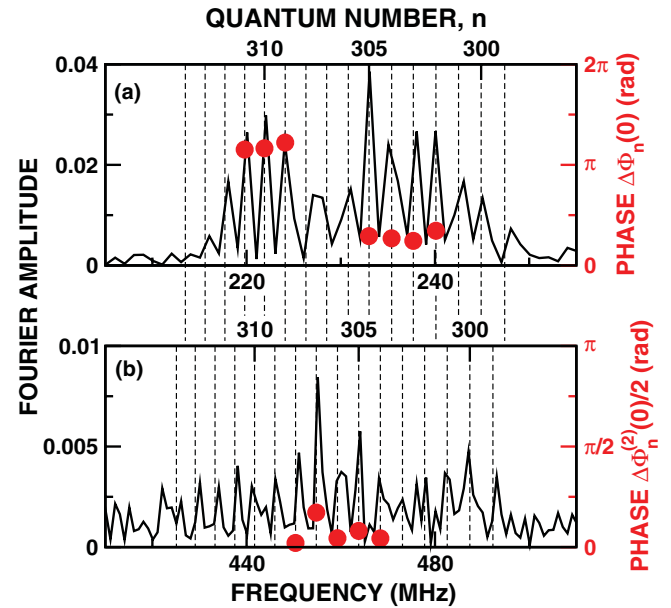

FIG. 6. (Color online) (a) and (b) Fourier transform of the survival probabilities shown in Figs. 5(a) and 5(b), respectively. The solid lines show the amplitudes of the Fourier expansion coefficients. The dots indicate the phases ϕ of the dominant peaks. Frequency is mapped to the quantum number n (indicated by the dashed lines) by $\omega_n = (n - 1/2)^{-3}$ and $\omega_n = 2n^{-3}$ for the first (a) and second (b) harmonics, respectively.

symmetric distribution is maintained during their time evolution, they contribute little to the time dependence of $\langle y(t) \rangle$. Only observation of the second harmonic renders them visible.

Careful inspection of the peak positions on the frequency axis reveals that the peaks associated with the second harmonics are not simply at twice the frequencies associated with the first harmonics. This results because the frequencies of the second harmonics $\Omega_n^{(2)} \simeq 2/n^3$ are defined by integer n, whereas the frequencies of the first harmonics given by $\Omega_n \simeq 1/(n - 1/2)^3$ in terms of half-integers, $n - 1/2$. This gives rise to the half-integer shift seen in Fig. 6 and is a direct manifestation of the relative phase shift between fractional revivals of different order [21,30].

VI. NARROWING THE *n*-DISTRIBUTION BY A HALF-CYCLE PULSE

With detailed information on the spatial distribution in a Bohr wave packet, in particular, the correlation between principal quantum number n and azimuthal angle ϕ, it is straightforward to design protocols to manipulate the wave packet. Here we demonstrate a protocol designed to change the width of the n distribution that is directly based on the n-ϕ correlation described above.

Consider the application of a half-cycle pulse (HCP), $F_{\text{HCP}}(t)$, with duration $T_p \ll T_n$ to an atom. This results in an impulsive momentum transfer, or "kick," to the electron given by

$$\Delta \vec{p} = - \int \vec{F}_{\text{HCP}}(t) dt, \qquad (20)$$

and an energy transfer

$$\Delta E = \vec{p}_i \cdot \Delta \vec{p} + O(\Delta p^2). \qquad (21)$$

For small HCP strengths ($|\Delta p| \ll |p_i|$) the electron gains or loses energy depending on the direction of its orbital momentum $\vec{p}_i$ at the time of HCP application. This momentum-dependent energy transfer provides the key to manipulating the n distribution of the (near-circular) wave packet. Consider an HCP that delivers a small kick in the $+y$ direction. Components of the wave packet initially located near the x axis moving in the $-y$ ($+y$) direction will lose (gain) energy, i.e., move to lower (higher) n. Components of the wave packet located near the y axis moving in the $+x$ or $-x$ directions will suffer little energy transfer. In all cases, since the HCP is small, only small changes in L_z occur. As demonstrated above, immediately following turn-off of the pump pulse the high-n ($n \sim 309$–311), and low-n ($n \sim 302$–305) components of the wave packet are located on opposite sides of the nucleus at $\phi \sim 3\pi/2$ and $+\pi/2$, respectively. The intermediate n components are positioned near $\phi \simeq 0$ and π. The application of a small kick (in the $+y$ direction) at this time will have little effect. The high- and low-n components remain essentially unchanged while the intermediate-n components, on average, suffer little net change in n because of their symmetrical distribution; i.e., each has components that move in the $+y$ and $-y$ directions. However, after a delay equal to one-quarter of a Kepler period the higher-n components are located on the $+x$ axis moving in the $+y$ direction, and the
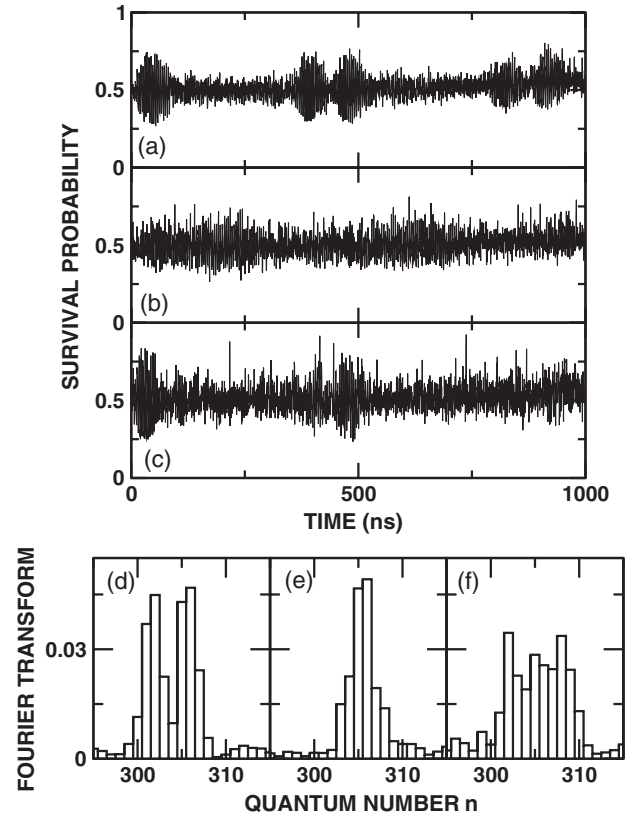

FIG. 7. (a) Survival probability measured following application of an 85-ns-long, 5 mV cm^{-1} pump pulse to a mix of quasi-1D $n_i \sim 305$ atoms and (d) its Fourier transform. The 6-ns-long probe pulse has an amplitude of 104 mV/cm. (b) and (c) Survival probabilities and (e) and (f) Fourier transforms obtained after application, following a delay of ~ 1.1 ns, of an HCP delivering a kick of scaled strength $\Delta p_0 \equiv n_i \Delta p = 0.007$ in the $-y$ and $+y$ directions, respectively (see text).

lower-n components are located on the $-x$ axis moving in the $-y$ direction. The intermediate-n components are positioned near the $+y$ and $-y$ axes. Thus the application of a kick in the $-y$ direction at this time can produce a significant narrowing of the n distribution as the higher-n components lose energy and the lower-n components gain energy. This is illustrated in Fig. 7 which shows the measured survival probabilities and Fourier amplitudes for a near-circular wave packet that is manipulated by an HCP. The initial near-circular wave packet is generated from a mix of $n_i = 304$ and 306 quasi-1D states using an 85 ns, 5 mV/cm pump pulse. Its subsequent evolution is monitored using a probe pulse and the time dependence in the survival probability is shown in Fig. 7(a) together with its distribution of Fourier components in Fig. 7(d). Figures 7(b) and 7(e) show the effect of the application of a small kick of 0.6 ns in duration and of scaled amplitude $\Delta p_0 = n_i \Delta p = 0.007$ in the $-y$ direction, 1 ns, i.e., one-quarter of an orbital period, after turn-off of the pump pulse. As seen in Fig. 7(b) the times associated with the growth and decay of the revivals become much longer indicating that fewer n levels are involved in the wave packet. Indeed, the Fourier transform [Fig. 7(e)] shows that the n distribution is substantially narrowed, its final width, $\Delta n \sim 2$,

approaching the limit of population of just a single n shell. As seen in Figs. 7(c) and 7(f), reversal of the kick direction leads to a broadening of the n distribution as the high-n (low-n) components now gain (lose) energy. In consequence, the initial localization and delocalization of the wave packet occur at earlier times when compared to the case where no HCP is applied.

VII. CONCLUSIONS

The dynamics of near-circular Bohr-like wave packets can be monitored by measuring the survival probability following the sudden application of a pulsed dc electric field. Because the probability of ionization depends on the initial position of the electron, information on its spatial distribution is encoded into the survival probability. Fourier analysis of the time-dependent survival probability yields the first and second moments of the

position coordinate, $\langle y^\lambda \rangle$ ($\lambda = 1,2$), and provides information on the distribution in azimuthal angle ϕ. This includes the average location of each n component, even when a single n component has a distribution with two localization peaks. Such information is critical for the design of protocols to further manipulate the wave packet.

[1] C. Ottaviani and D. Vitali, Phys. Rev. A **82**, 012319 (2010).

[2] S. Gleyzes, S. Kuhr, C. Guerlin, J. Bernu, S. Deleglise, U. B. Hoff, M. Brune, J. Raimond, and S. Haroche, Nature (London) **446**, 297 (2007).

[3] M. Brune, F. Schmidt-Kaler, A. Maali, J. Dreyer, E. Hagley, J. M. Raimond, and S. Haroche, Phys. Rev. Lett. **76**, 1800 (1996).

[4] E. Hagley, X. Maître, G. Nogues, C. Wunderlich, M. Brune, J. M. Raimond, and S. Haroche, Phys. Rev. Lett. **79**, 1 (1997).

[5] M. Gross and J. Liang, Phys. Rev. Lett. **57**, 3160 (1986).

[6] A. Nussenzweig, J. Hare, A. M. Steinberg, L. Moi, M. Gross, and S. Haroche, Europhys. Lett. **14**, 755 (1991).

[7] C. H. Cheng, C. Y. Lee, and T. F. Gallagher, Phys. Rev. Lett. **73**, 3078 (1994).

[8] J. C. Day, T. Ehrenreich, S. B. Hansen, E. Horsdal-Pedersen, K. S. Mogensen, and K. Taulbjerg, Phys. Rev. Lett. **72**, 1612 (1994).

[9] J. Hare, M. Gross, and P. Goy, Phys. Rev. Lett. **61**, 1938 (1988).

[10] R. Lutwak, J. Holley, P. P. Chang, S. Paine, D. Kleppner, and T. Ducas, Phys. Rev. A **56**, 1443 (1997).

[11] D. Delande and J. C. Gay, Europhys. Lett. **5**, 303 (1988).

[12] J. J. Mestayer, B. Wyker, J. C. Lancaster, F. B. Dunning, C. O. Reinhold, S. Yoshida, and J. Burgdörfer, Phys. Rev. Lett. **100**, 243004 (2008).

[13] S. Yoshida, C. O. Reinhold, J. Burgdörfer, B. Wyker, and F. B. Dunning, Phys. Rev. A **81**, 063428 (2010).

[14] N. Bohr, Philos. Mag. **26**, 1 (1913).

[15] B. E. Tannian, C. L. Stokely, F. B. Dunning, C. O. Reinhold, and J. Burgdörfer, Phys. Rev. A **64**, 021404 (2001).

[16] I. S. Averbukh and N. F. Perelman, Phys. Lett. A **139**, 449 (1989).

[17] R. Bluhm and V. A. Kostelecký, Phys. Rev. A **51**, 4767 (1995).

[18] C. O. Reinhold, S. Yoshida, J. Burgdorfer, B. Wyker, J. J. Mestayer, and F. B. Dunning, J. Phys. B **42**, 091003 (2009).

[19] H. Goto, H. Katsuki, H. Ibrahim, H. Chiba, and K. Ohmori, Nat. Phys. **7**, 383 (2011).

[20] R. R. Jones, D. You, and P. H. Bucksbaum, Phys. Rev. Lett. **70**, 1236 (1993).

[21] Z. D. Gaeta and C. R. Stroud Jr., Phys. Rev. A **42**, 6308 (1990).

[22] F. B. Dunning, C. O. Reinhold, S. Yoshida, and J. Burgdörfer, Am. J. Phys. **78**, 796 (2010).

[23] E. A. Shapiro, Sov. Phys. JETP **91**, 449 (2000).

[24] R. R. Jones and M. B. Campbell, Phys. Rev. A **61**, 013403 (1999).

[25] J. Ahn, D. N. Hutchinson, C. Rangan, and P. H. Bucksbaum, Phys. Rev. Lett. **86**, 1179 (2001).

[26] D. Richards, J. Phys. B **17**, 1221 (1984).

[27] J.-C. Gay, D. Delande, and A. Bommier, Phys. Rev. A **39**, 6587 (1989).

[28] C. Lena, D. Delande, and J. C. Gay, Europhys. Lett. **15**, 697 (1991).

[29] C. L. Stokely, J. C. Lancaster, F. B. Dunning, D. G. Arbó, C. O. Reinhold, and J. Burgdörfer, Phys. Rev. A **67**, 013403 (2003).

[30] P. Kasperkovitz and M. Peev, Phys. Rev. Lett. **75**, 990 (1995).